The Astrophysical Journal Letters, 992:L23 (11pp), 2025 October 20 https://doi.org/10.3847/2041-8213/ae0df2

Fine Structures of Tiny Quiet Sun Jets Observed by Solar Orbiter and Big Bear Solar Observatory

Jeongwoo Lee[1,2,3], Dana Longcope[4], Junmu Youn[5], Navdeep K. Panesar[6,7], Nengyi Huang[1,2,3], and Haimin Wang[1,2,3]
[1] Institute for Space Weather Sciences, New Jersey Institute of Technology, University Heights, Newark, NJ 07102, USA; leej@njit.edu
[2] Center for Solar-Terrestrial Research, New Jersey Institute of Technology, University Heights, Newark, NJ 07102, USA
[3] Big Bear Solar Observatory, New Jersey Institute of Technology, 40386 North Shore Lane, Big Bear City, CA 92314, USA
[4] Department of Physics, Montana State University, Bozeman, MT 59717, USA
[5] School of Space Research, Kyung Hee University, Yongin 17104, Republic of Korea
[6] Lockheed Martin Solar and Astrophysics Laboratory, 3251 Hanover Street, Building 203, Palo Alto, CA 94306, USA
[7] SETI Institute, 339 Bernardo Avenue, Mountain View, CA 94043, USA

Received 2025 August 22; revised 2025 September 17; accepted 2025 September 29; published 2025 October 14

Abstract

We present the first joint high-resolution observations of small-scale EUV jets using Solar Orbiter (SolO)'s Extreme Ultraviolet Imager and High Resolution Imager (EUI/HRI$_{\rm EUV}$) and Hα imaging from the Visible Imaging Spectrometer installed on the 1.6 m Goode Solar Telescope at the Big Bear Solar Observatory. These jets occurred on 2022 October 29 around 19:10 UT in a quiet Sun region, and their main axis aligns with the overarching magnetic structure traced by a cluster of spicules. However, they develop a helical morphology, while the Hα spicules maintain straight, linear trajectories elsewhere. Alongside the spicules, thin, elongated red- and blueshifted Hα features appear to envelope the EUV jets, which we tentatively call sheath flows. The EUI jet moving upward at a speed of $\sim$110 km s^{-1} is joined by a strong Hα redshift at $\sim$20 km s^{-1} to form bidirectional outflows lasting $\sim$2 minutes. Using AI-assisted differential emission measure analysis of SolO's Full Sun Imager, we derived total energy of the EUV jet as $\sim 1.9 \times 10^{26}$ erg with 87% in thermal energy and 13% in kinetic energy. The parameters and morphology of this small-scale EUV jet are interpreted based on a thin flux tube model that predicts Alfvénic waves driven by impulsive interchange reconnection localized as narrowly as $\sim$1.6 Mm with a magnetic flux of $\sim 5.4 \times 10^{17}$ Mx, belonging to the smallest magnetic features in the quiet Sun. This detection of intricate corona–chromospheric coupling highlights the power of high-resolution imaging in unraveling the mechanisms behind small-scale solar ejections across atmospheric layers.

Unified Astronomy Thesaurus concepts: Jets (870); Quiet sun (1322); Solar chromosphere (1479); Alfven waves (23); Solar magnetic reconnection (1504)

Materials only available in the online version of record: animations

1. Introduction

Small-scale ejections/eruptions (SSEs) in the low solar atmosphere are believed to play an important role in the energy balance, mass loading, and fine structuring of the solar corona as well as mass transport into the solar wind (J. Lee et al. 2022; A. C. Sterling et al. 2024; N. Bizien et al. 2025). Many of these small-scale events are observed in a variety of forms of jets, which may provide the upward flux of mass, momentum, and energy necessary for the observed heating and flows (N. K. Panesar et al. 2023; F. Shi et al. 2024). However, the connections among the different types of SSEs, especially those in different layers of the atmosphere, remain obscure (F. Shi et al. 2024). Improved physical understanding of the formation of and the mechanisms behind the jetting phenomenon is fundamentally important within the broad field of heliophysics (Y. Shen 2021). Such works could help synthesize the disparate observations and theories of SSEs into a more cohesive, coherent framework.

SSEs are characterized by well-collimated ejecta apparently flowing along preexisting magnetic field lines. First discovered in *Skylab* He II 304 Å images as cool ($\sim 8 \times 10^4$ K) plasma ejections in coronal holes (J. D. Bohlin et al. 1975), macrospicules appear to be giant spicules or small surges (J. M. Beckers 1977; E. Tandberg-Hanssen 1977). They extend 7000–40,000 km above the limb, with a rising velocity of 10–150 km s^{-1} and a lifetime of 3–45 minutes (K. P. Dere et al. 1989b; M. Karovska & S. R. Habbal 1994). Using data from Big Bear Solar Observatory (BBSO), Hα macrospicules were found to be associated with EUV macrospicules and X-ray-bright point flares (R. L. Moore et al. 1977). Later work (Y. Yamauchi et al. 2004, 2005) showed that macrospicules exhibit two different forms: an erupting loop containing a minifilament (see below) and a single-column spiked jet. The relationship between macrospicules and other SSEs is unclear, particularly since previous studies were focused on limb events for which no magnetic field measurements were available.

Higher in the atmosphere, observations in UV spectral lines reveal the presence of similar kinds of ejections in the transition region (TR). Impulsive bidirectional and unidirectional high-speed flows denoted "explosive events" and "coronal bullets" were first detected in UV spectra by the High Resolution Telescope and Spectrograph (J. W. Cook et al. 1983) rocket-borne instrument (G. E. Brueckner 1982) and attributed to magnetic reconnection in the network (K. P. Dere et al. 1989a). Analyzing Si IV 1402.77 Å line data from the Interface Region Imaging Spectrograph (IRIS; B. De Pontieu et al. 2014), a prevalence of intermittent small-scale

TR jets with speeds of 80–250 km s^{-1} originating from the narrow bright network lanes was found (H. Tian et al. 2014). These jets have lifetimes of 20–80 s and widths of $\leqslant$300 km and are rooted in small-scale bright regions, often preceded by footpoint brightenings and accompanied by transverse waves with 20 km s^{-1} amplitudes. Many TR jets reach temperatures of at least 10^5 K and constitute an important element of the TR structure. As with type II spicules and macrospicules, we propose to explore the relationship between TR jets and other SSEs.

Coronal jets are commonly found in coronal holes, quiet Sun regions, and the peripheries of active regions. First detected in soft X-ray images by Yohkoh (e.g., K. Shibata et al. 1992), coronal jets have since been observed in the EUV, hard X-rays, white light (via coronagraphs), and microwaves, with speeds of ∼100–400 km s^{-1} and sizes of ∼5–500 Mm (N. E. Raouafi et al. 2016). Small-scale jetting activity, also called jetlets (N.-E. Raouafi & G. Stenborg 2014; N. K. Panesar et al. 2018), has received attention for its possible connection to solar wind transients, including switchbacks (N. E. Raouafi et al. 2023). Recent studies, using data from Solar Orbiter (SolO; D. Müller et al. 2020), have turned to even smaller-scale ejections, campfires, probably the smallest class of EUV jets observed in the corona (D. Berghmans et al. 2021; N. K. Panesar et al. 2021, 2023), providing unprecedented insights into these fine-scale phenomena.

A new opportunity for studying fine-scale SSEs is available with SolO in collaboration with Goode Solar Telescope (GST) at BBSO. SolO includes the Extreme Ultraviolet Imager (EUI), which offers high-resolution images through the High Resolution Imager (HRI$_{\rm EUV}$) at 174 Å with a pixel resolution of <0$''$.5 (P. Rochus et al. 2020; D. Berghmans et al. 2021), which corresponds to 100 km on the Sun during the perihelion observations (P. Rochus et al. 2020). L. P. Chitta et al. (2023) reported so-called picoflare jets on scales of a few hundred kilometers and speeds of ∼100 km s^{-1} detected by the EUI/HRI$_{\rm EUV}$, which would be one of the smallest-scale jets. E. Petrova et al. (2024) found a tiny helical flux rope at propagation speeds of 136–160 km s^{-1} using the Spectral Imaging of the Coronal Environment (SPICE) instrument and the Polarimetric and Helioseismic Imager on board SolO. On the ground, the 1.6 m, high-order adaptive-optics-equipped GST at BBSO can achieve a resolution as high as 0$''$.1–0$''$.2 with a pixel size of 0$''$.029, ideal for studying small-scale physical processes in the photosphere and chromosphere (P. R. Goode et al. 2010). Time series of Hα imaging spectroscopy with multiple wavelength points provide the Fabry–Pérot-based Visible Imaging Spectrometer (VIS) of high image quality (e.g., T. Samanta et al. 2019). Such SolO–BBSO joint observations allow us to address the key issue of SSEs: what dictates the structure and dynamics of the SSEs and what role the magnetic reconnection has in SSEs in the photosphere, chromosphere, and corona.

2. Data and Analyses

On 2022 October 29, the GST was pointing to a quiet Sun region (201$''$E, 356$''$N) that was also within the field of view (FOV) of SolO's EUI/HRI$_{\rm EUV}$. During the coordinated observation, EUI/HRI$_{\rm EUV}$ detected two small-scale jets in quick succession at 19:07:30 UT and 19:13:30 UT at the position of SolO. SolO was located at 0.46 au, resulting in a photon arrival time difference of 4.5 minutes with respect to the Solar Dynamics Observatory (SDO) and BBSO. SolO had angular separation from the SDO by 37°.9 so that the target in the east quadrant in the Atmospheric Imaging Assembly (AIA) view appears in the west quadrant in SolO's view (Figure 1). We were unable to find, in SolO's SPICE data, significant Doppler signals at the jet location, likely due to either weak emission or the large inclination angle of the jets relative to the line of sight (LOS). Hα pseudo-Dopplergrams are constructed from the GST/VIS images at five wavelength points: H$\alpha \pm 0.8$ Å, H$\alpha \pm 0.4$ Å, and the line center. We used the center-of-gravity method, which utilizes the residual intensity profile, the difference between the line profile and the reference profile. Depending on which reference profile is used, two types of Doppler speed may result. Use of the ambient continuum intensity as the reference (H. Uitenbroek 2003) gives higher weights to the line core, resulting in low speeds. If we use the mean spectrum of the whole FOV (L. Rouppe van der Voort et al. 2009), more weight is given to the wing enhancement, resulting in higher speeds. The latter method was used in this study.

2.1. SolO/EUI, SDO/AIA, and GST/VIS Images

Figure 1 presents the SDO/AIA 171 Å image (a) and the EUI/HRI$_{\rm EUV}$ image in a larger FOV (b), including NOAA AR 13133 itself, in the top panels, where our target jet is marked with a white box. Zoom-in views of the jet seen by three different instruments are plotted in the bottom four panels ((c)–(f)) along with an overlay of Hα and EUV images in (g). The three colored curves and the warped rectangles marking NOAA AR 13133 are not the present target but are plotted to check the different projection effects on both images. They are coordinate-transformed from the half-circles tilted at three angles and a straight rectangle in the disk center to the positions of AIA and EUI/HRI$_{\rm EUV}$ to demonstrate the different orientations of the two loops in the SDO and SolO images. Our target is a tiny EUV jet that emerged suddenly from the dark corona around 19:10 UT within the region marked with the box located north of the active region. The main parts of this jet are obscured by an EUV loop in the foreground in SDO/AIA (a) but could be directly detected from the different perspective of SolO (b). For the direct comparison with AIA images, we adjusted the tilt angle of the EUI/HRI$_{\rm EUV}$ 174 Å according to the above practice of the projection on different locations on the disk (c). The blue contours outlining the profiles of the AIA image are taken from (d) and copied to other panels ((c), (e), and (f)). The EUI/HRI$_{\rm EUV}$ image reveals the fine-scale helical pattern of EUV-bright strands giving an impression of twisted field lines or flux ropes (c). The jet's fine structure is less clearly visible in the AIA 171 Å image (d), although AIA 171 Å images usually look similar to the EUI 174 Å images (e.g., S. Mandal et al. 2023). The different appearance can be partly due to the lower spatial resolution of AIA, or the accidental blockage of the jets by a foreground EUV-bright structure in AIA's FOV might be another factor. We must also note that the EUV structures appear as different shapes depending on the observer's different perspective, as previous differential emission measure (DEM) studies comparing SDO/AIA and SolO/Full Sun Imager (FSI) data have demonstrated (J. Youn et al. 2025).

The GST/VIS's inverted Hα blue wing (e) and red wing (f) images exhibit the spicules in straight trajectories without any

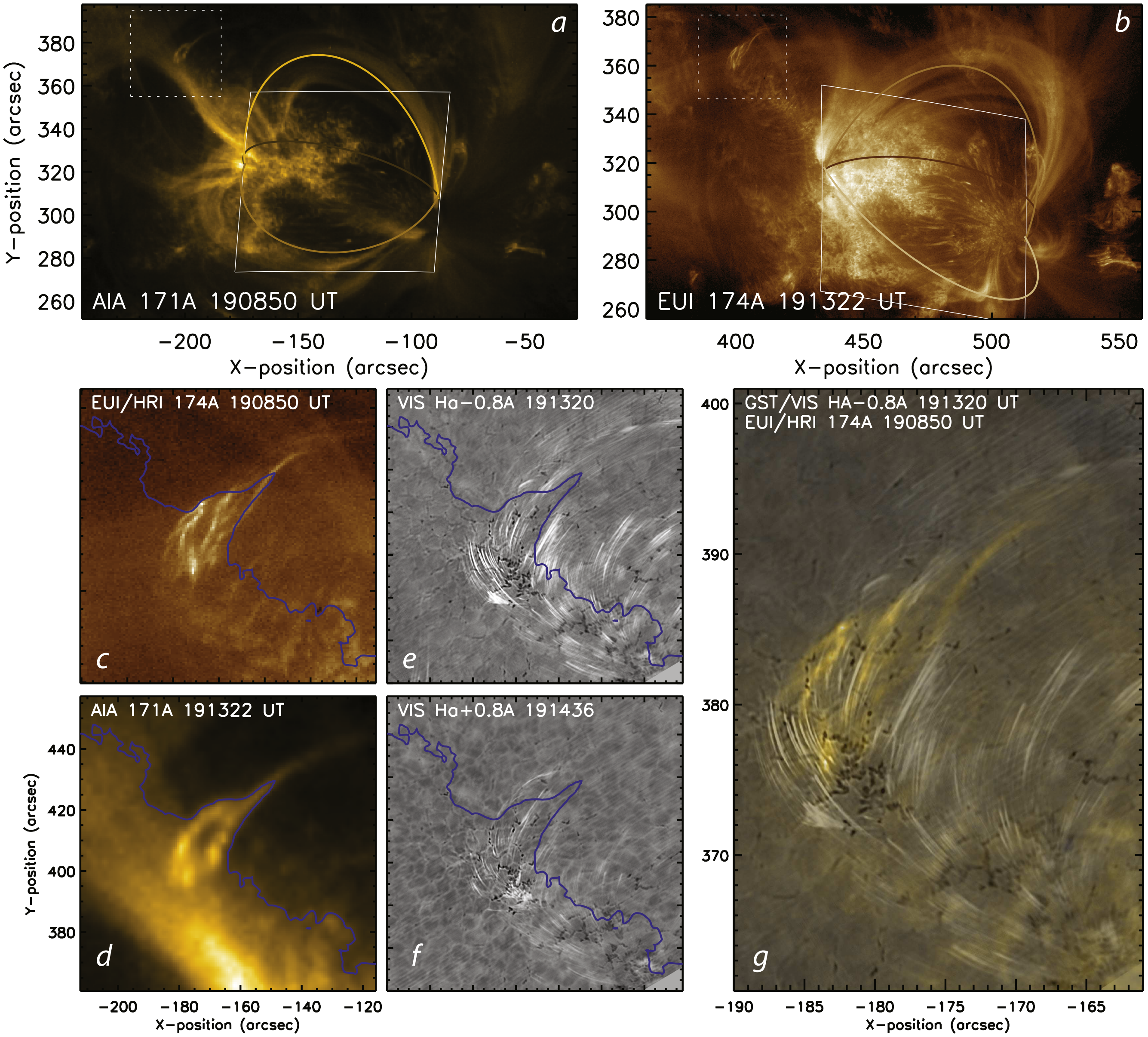

Figure 1. Projection effects of the quiet-region EUV jet for multiple instruments. (a) SDO/AIA 171 Å with a small jet enclosed by the dotted box. (b) SolO's EUI/HRI$_{\mathrm{EUV}}$ 174 Å of the same region. The three-color half-circles are meant to show the projection effect. Model loops are constructed in the disk center and projected back to the two locations. Other images in the small FOV around the jets shown in (c)–(e) include a tilt-adjusted EUI/HRI$_{\mathrm{EUV}}$ 174 Å (c), the SDO/AIA 171 Å (d), and Hα wing ±0.8 Å images ((e) and (f)). As a reference, we overlay the outline of the AIA 171 Å profile (blue contour from (d)) on other images ((c), (e), and (f)). A composite image of the Hα blue wing image (gray scale) and EUI/HRI$_{\mathrm{EUV}}$ in yellow color shades (g) shows different morphologies. The observation time of AIA and GST is delayed by 4.5 minutes from that of EUI/HRI$_{\mathrm{EUV}}$.

helical structure of the EUV jets. A composite image of the Hα blue wing image (gray scale) and EUI/HRI$_{\mathrm{EUV}}$ in yellow color shades (g) shows the obvious difference that the Hα spicules move along straight trajectories and the EUI/HRI$_{\mathrm{EUV}}$ 174 Å structures are twisted. In addition, there are differences in spatiotemporal distribution. The EUV jets occurred in a small area ($\sim$3 Mm) and lasted only $\sim$2 minutes in the region that is otherwise EUV-dark, while the spicules are numerous and constantly occurring elsewhere at an enormously different rate. All of these differences should arise from the intrinsic properties in both radiations and are hardly due to either the projection effect or resolution. As an additional note, no jet bright point (JBP; A. C. Sterling et al. 2016) is found, implying that the EUV jet only occurred up in the corona without leaving traces in the lower atmosphere. In that sense, this jet is similar to some of the Hi-C jets (N. K. Panesar et al. 2019) that occurred at the edges of the magnetic network lanes.

2.2. EUV Jets and Spicules

In Figure 2, we make one-to-one comparisons of the EUV jet with those of Hα spicules during their evolution. These jets are highly inclined, and we nonetheless plot them with their axis up for visual convenience. The top panels show a sequence of the EUI/HRI$_{\mathrm{EUV}}$ images at the time of the first jetting, 19:07 UT–19:10 UT, alongside the GST Hα far wing difference images in the middle and Hα Dopplergrams in the bottom. Initially (before 19:07 UT in SolO time), a faint, weakly curved flux-tube structure became apparent, showing a distinct brightening in its central part to form a wedge-like

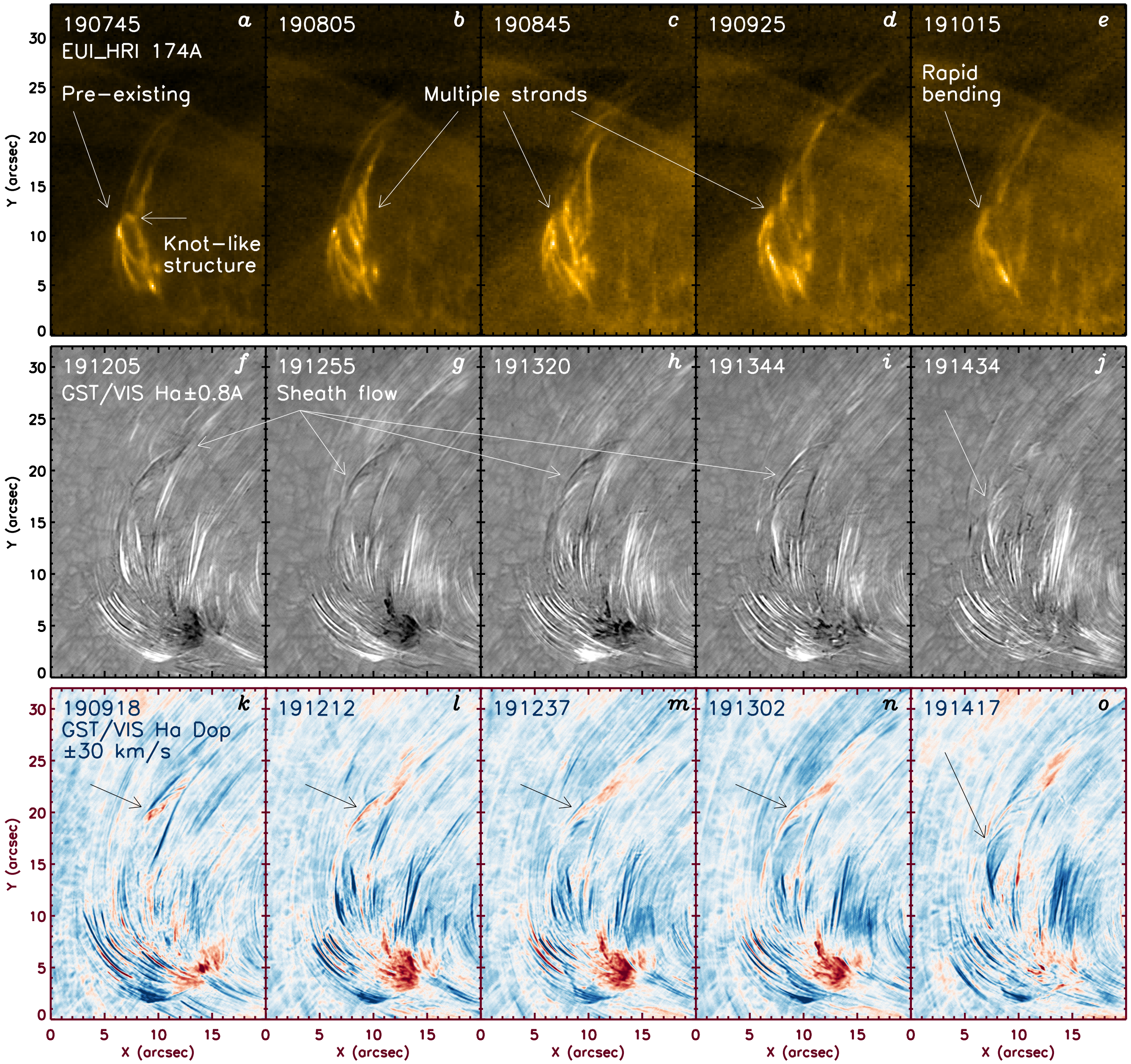

Figure 2. The evolution of EUI/HRI$_{\mathrm{EUV}}$ jet structure at 174 Å (top), the difference between Hα ±0.8 Å wing images (middle), and pseudo-Dopplergrams from five wavelength point GST/VIS images (bottom). They show a preexisting strand (a), a knot-like structure (b), multiple stripes ((b)–(d)), and a rapidly turning or bending structure ((e), (j), (o)) as well as sheath flows (arrows in (f)–(i) and (k)–(n)). The Dopplergrams show strong redshift components concentrated under the EUV jets.

structure and further evolves into a knot-like structure (a). This is suggestive of interchange reconnection in appearance. The twisted structure with a single strand develops into multiple strands (b) and three prominent stripes at the maximum intensity (c). Their separation increases as they propagate away (d) and finally disappear (e). We also see the points where the jet's guiding field lines rapidly turn around (d); it is either the curved jet structure or some other background structure. In about 4 minutes, the jet diminishes and a faint, rapidly bending structure appears in the flank of the EUV jet (e).

The middle panels show the red wing to blue wing difference Hα ±0.8 Å images at the corresponding times taking into account the relative time delay between EUI/HRI$_{\mathrm{EUV}}$ and GST. One similar feature of the Hα images with the EUI/HRI$_{\mathrm{EUV}}$ images is that the strand in (f) coincides well with the preexisting EUV structure (a). The multiple EUV stripe pattern is not exactly reproduced in the Hα images, but an alternating thin blue and red wing feature as thin as 200 km is found near the boundary of the EUV jets ((f)–(i)). Given their spatial association with the jet, we tentatively call it "sheath flow," which may be cold plasma enveloping the hot EUV jet stream. The sheath flow is aligned toward the EUV jet spire with different characteristics from typical spicules. Later, the sheath flow shrinks down to a lower height (j), although it does not exactly coincide with the rapidly bending EUV jet structure (e). They are therefore not the same phenomena.

The sheath flow is a new phenomenon requiring further interpretation. In this simple picture, the EUV-bright and dark regions correspond to the corona and chromosphere, respectively.

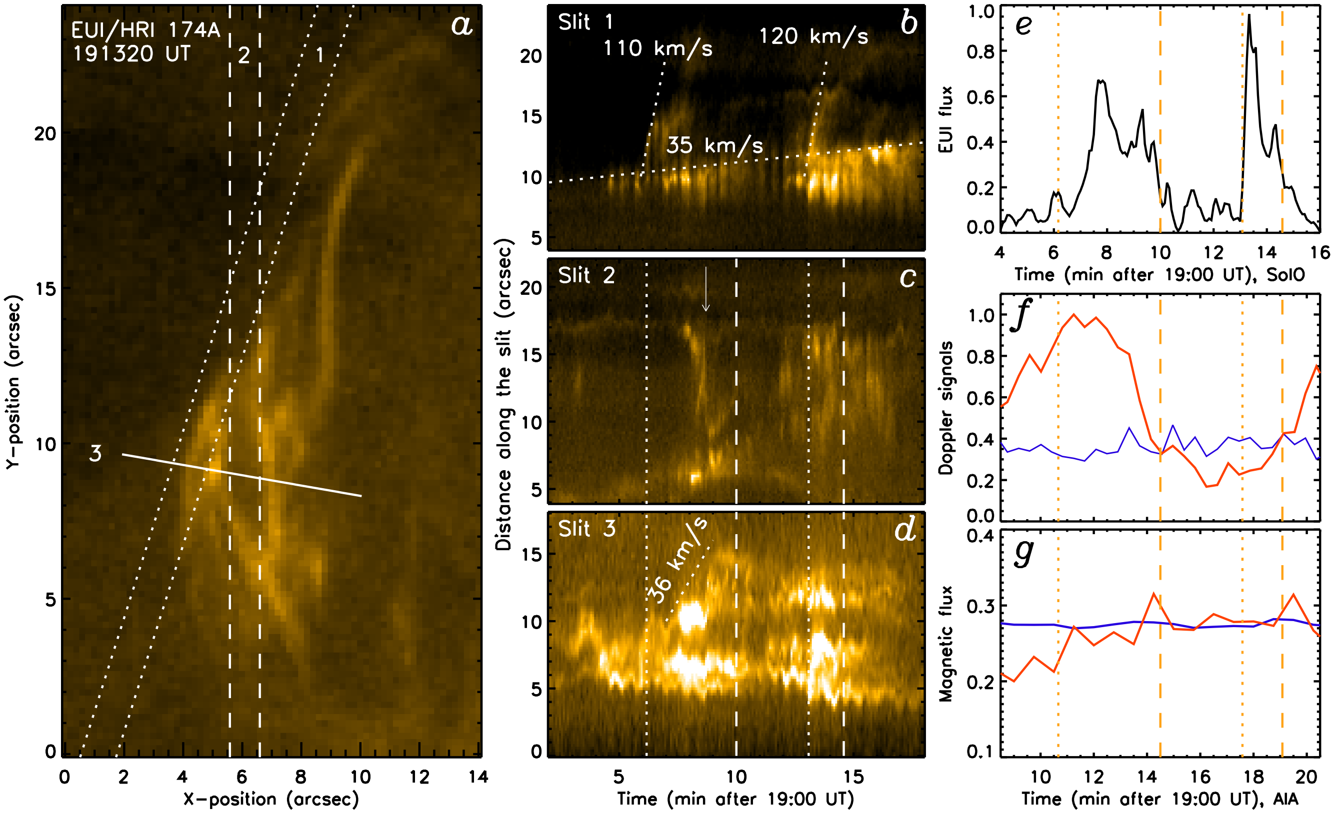

Figure 3. EUV TD maps and time profiles of EUV flux, Hα Doppler motions, and magnetic flux. (a) An EUI/HRI$_{\mathrm{EUV}}$ image with slit positions set for the TD maps. (b)–(d) TD maps for EUI along slits 1–3 show upward speeds of 110–120 km s^{-1} and the evolving helical structure (white arrow). Time profiles of the (e) EUV flux, (f) Hα Doppler shift fluxes, and (g) magnetic fluxes. In (g), the red (blue) curve corresponds to the positive (negative) flux. In (c)–(g), the vertical lines indicate the start (dotted lines) and end (dashed lines) times of the two jets. The animation of panel (a) is from 19:00:00 UT to 19:21:40 UT.

(An animation of this figure is available in the online article.)

The sudden appearance of an EUV jet within a dark region is thus regarded as the formation of a localized corona embedded within the chromosphere rather than above the chromosphere. This structure likely introduces a thin interface between the hot jet and the surrounding chromospheric plasma that forms due to insufficient time for a full exchange of particles and energy between them. Nearby spicular flows will be sliding along the sheath instead of penetrating the jet region, like a tangential flow along an impermeable wall, and thus called sheath flow. Other uprising spicules are also in the straight trajectory, in contrast with the helical EUV jet structure. We should also note that the Hα spicules are constantly regenerating, whereas the EUV helical structure lasts over a short period of ~2 minutes.

The Dopplergrams in the bottom panels show the sheath flows more clearly (arrows in (k)–(n)), which could imply torsional motion of cool plasma around the EUV jets. The spray feature in the Hα wing difference image (j) appears as a blueshift component in the Dopplergram (o). The Hα spray feature does not exactly coincide with the rapidly bending EUV structure (e) and may be a sheath flow too. Otherwise, the blueshift component dominates ((f)–(h)), and those in thin and long structures are upward spicules. The redshifted Hα components may also be spicules directed downward, but they are timely correlated with the EUV jets, unlike other normal spicules, and are highly concentrated in the presumed location of the EUV jet footpoint. We suggest that they could instead be the downward outflow from the reconnecting X-point associated with the EUV jets. Their speeds reach ~20 km s^{-1} and join the EUV jets in the opposite direction. The Hα redshift is therefore an important component that connects the EUV coronal jets down to the photospheric magnetic fields.

2.3. Dynamics of EUV Jets

We focus on investigating the dynamics of the EUV jets using time–distance (TD) maps, which provide estimates of transverse motions. Figure 3 presents TD maps along four slits and related time profiles. Slit 1, aligned with the most persistent structure, allows an easy measurement of the linear upward motion: the first (19:06 UT) and second (19:13 UT) jets exhibit upward speeds of ~110 km s^{-1} with a baseline increasing more slowly at ~35 km s^{-1}. However, this slope can be underestimated due to the finite inclination angle. Therefore, the upward EUV jets and the downward Hα materials have enormously different speeds. Slit 2 set parallel to the jet axis and passing through the first jet finds a fast twisting feature at (19:08 UT). Slit 3, positioned orthogonally across the jet axis, detects the width of the jet and shows the pronounced expansion occurring primarily during the first jet. The jets expands in width from 2 to 5 Mm for the 3 minute period, after which the structure remains stable in size through the second jet.

In the rightmost column, we compare the time profiles of the EUI 174 Å flux, the area-integrated Hα Doppler signal, and the magnetic flux with each other. Due to the SolO–AIA position difference, the EUI 174 Å flux peaks at 19:07:30 UT and 19:13:30 UT appear at the SDO position, with the photon arrival time delayed by 4.5 minutes. During the first peak, the EUV flux peak coincides with that of the area-integrated Hα

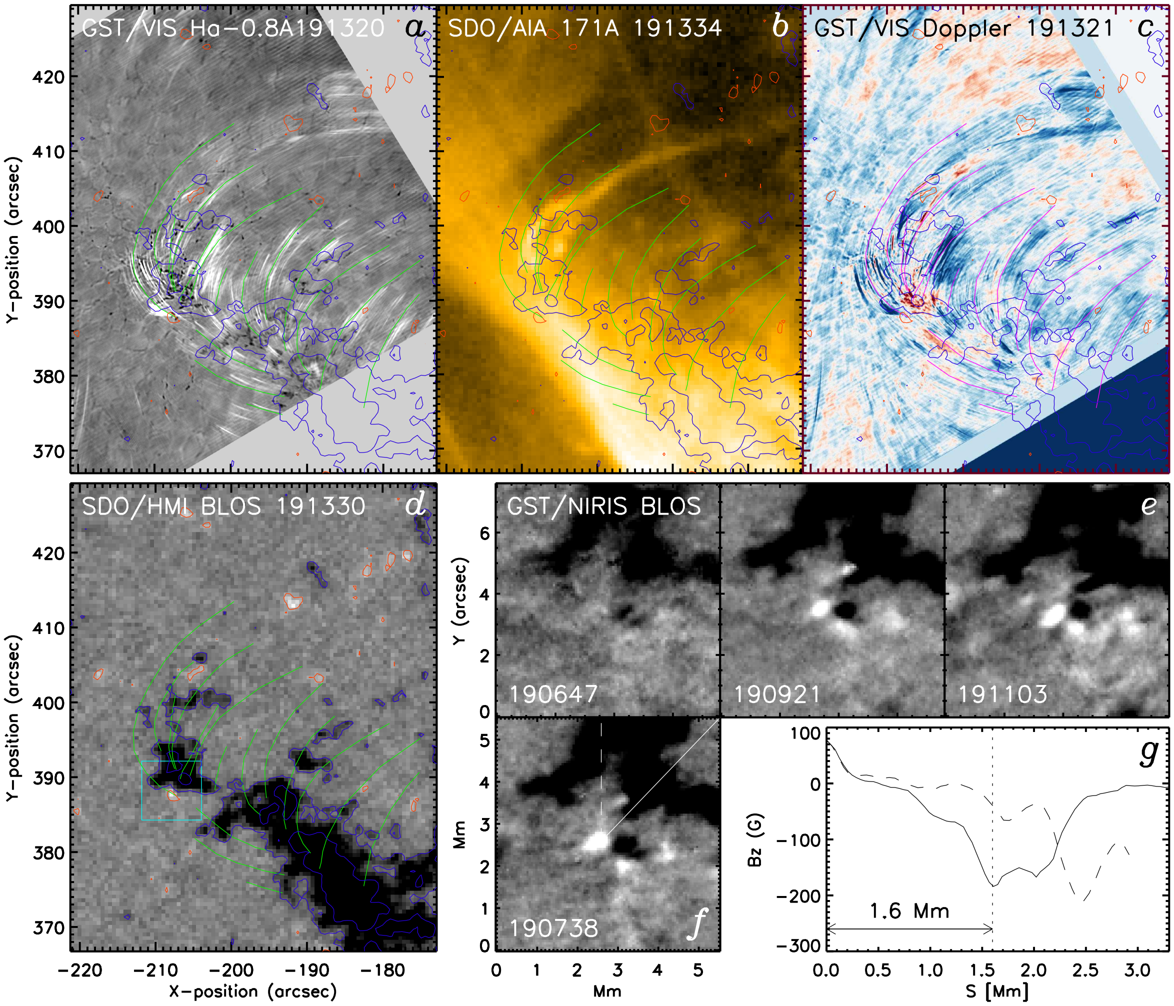

Figure 4. Correspondence between the magnetic fields, spicules, and EUV jet. (a) The Hα spicule trajectory readouts (green lines) from the GST/VIS −0.8 Å image are taken as a proxy for the magnetic field lines and copied to (b)–(d). (b) SDO/AIA 171 Å image with the LOS magnetogram (contours). (c) Same as (a) over the Dopplergram with the blue/red colors representing blueshift and redshift. The field lines are colored magenta in this panel. (d) An SDO/HMI LOS magnetogram with the contours at the levels of −40 G (blue) and +30 G (red). These contours are overplotted in panels (a)–(c) as well. (e) The three panels are GST/NIRIS LOS magnetic fields in the small FOV (cyan box in (d)) in units of arcseconds. (f) NIRIS magnetogram in the same FOV at another time in units of Mm. Two guide lines are the slits for scanning the 1D magnetic field distributions. (g) Distribution of the vertical magnetic field, B_z, read along the two slits. The animation shows panels (a) and (c) from 19:06:16 UT to 19:20:55 UT.

(An animation of this figure is available in the online article.)

redshift signal, although the redshift flux tends to precede the EUV flux enhancement. This correlation between EUV jets and Hα redshifts is missing for the second EUV jet. Another difference from the first jets is that the EUV-bright strands in the second jets are structured like straight flux tubes aligned with the Hα spicules. The magnetic fluxes measured from the Helioseismic and Magnetic Imager (HMI) magnetograms (see Figure 4) show that the negative polarity magnetic flux remains largely stable, while the parasitic positive flux steadily increases after its emergence covering the period of the first jets. No such trend is seen for the second EUV peak. Therefore, the first and second EUV jets differ from each other in morphology and correlation with the Hα Doppler signals and magnetic flux, implying different driving mechanisms for the two EUV jetting events.

2.4. Magnetic Fields around the EUV Jets

The target region in the photosphere is dominated by the negative polarity, and the positive polarity is scattered around in small patches. Another small positive polarity flux emerges before the jet time, which is likely to be associated with the jetting. We attempt to infer the overall magnetic connectivity from the Hα spicule trajectory assuming they follow the magnetic field to some extent. In Figure 4(a), we plot the GST/VIS Hα blue wing image so that the spicules appear as the white narrow features and the HMI LOS magnetic field as contours. The green curves are readouts of the spicule trajectories from the Hα blue wing image, which are then copied to the AIA 171 Å intensity image (Figure 4(b)) and the HMI LOS magnetogram itself (Figure 4(d)) and as magenta lines on the Dopplergram (Figure 4(c)). The spicule trajectories (green curves) outline the magnetic field stemming from the negative polarity flux running toward the positive polarity patch far off in the north.

An important implication of the Hα spicule trajectories would be that they map the magnetic field lines connecting the EUV jet base to the photosphere and that of the EUV jet spire to remote regions. With the AIA image alone, we do not see the EUV jet reach down to the emerging positive flux patch. However, the EUI/HRI$_{\mathrm{EUV}}$ images show the EUV jet

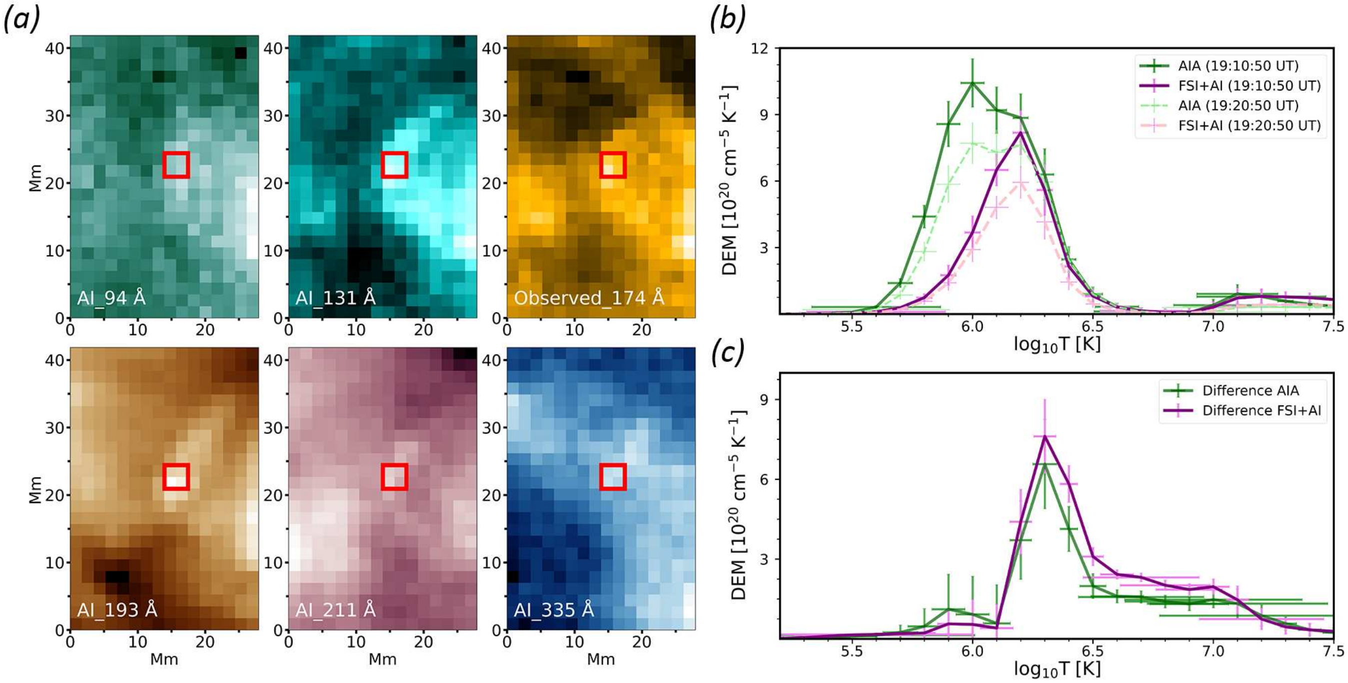

Figure 5. DEMs of the jet region derived from EUV images. (a) The six panels show one EUI/FSI 174 Å image and five AIA-equivalent images generated by deep learning. The red box indicates the pixels used to calculate the DEM. (b) The DEM derived from the SDO/AIA images (green) with AI-generated EUV images with the observed FSI 174 Å image (purple). The solid lines represent the DEM profiles when the jet activity is strong (19:10:20 UT), while the dashed lines correspond to the profiles when the jet diminished (19:20:50 UT). (c) The net DEM calculated from the difference EUV images between the jet maximum and the jet quiet time.

being extended further south, and the Hα spicule trajectories indicate the magnetic field lines rapidly wrapped toward the positive flux patch underneath. Furthermore, the redshifted Hα components are densely packed under the EUV jets as if they are Hα counterparts of JBPs. The upward trajectory of the EUV jet also follows this curved path of the Hα spicules as shown in Figure 4(b). Of course, not all field lines are exactly parallel to each other, with inclination angles varying with position to some extent, but the overall EUV jet trajectories tend to follow the westward structure implied by the Hα spicules. The westward wrapping structure is also obvious in the Dopplergram (Figure 4(c)). The field lines stemming from the positive flux patch seem to be the outermost of this overarching magnetic structure.

The HMI magnetogram in Figure 4(d) shows a few positive polarity patches in the north. They are probably connected to the negative flux region to form an arcade-like structure, as implied by the spicule trajectories. A large patch in the positive polarity exists in the east, but these field lines are connected to the east in view of the Hα images. Beneath the EUV jets, the photospheric magnetic fields were of negative polarity alone, but at 19:06 UT, a small positive flux patch emerged in the south (within the cyan box), and the EUV jets started.

Figure 4(e) shows an NIRIS magnetogram in the small FOV indicated by the cyan box in Figure 4(d) in order to investigate the evolution of the positive polarity patch. This small structure is not clearly visible in the HMI magnetogram because of the limited resolution and sensitivity. With the emergence of the small positive flux patch at ∼19:07 UT, it becomes a mixed polarity region. The positive polarity flux kept increasing without an obvious signature of magnetic flux cancellation. When it converged toward the PIL, the jets occurred. In Figure 4(f), we set two slits (solid and dashed) to read out the 1D magnetic profiles shown in Figure 4(g). The field strength corresponds to the local vertical magnetic field, B_z, obtained by dividing the LOS magnetic field by $\cos\theta$ with the position angle $\theta = 27^\circ$ from the disk center. The separation between a nearby bipolar pair is estimated as 1.6 Mm, and their peak strengths are +80 G and −180 G, respectively, indicating that it is one of the typical smallest SSEs (C. E. Parnell et al. 2009; J. Lee et al. 2025).

2.5. Plasma Properties and Energies of the EUV Jets

The temperature and electron density diagnostics for the EUV features are usually available from the DEM analysis of SDO/AIA (I. G. Hannah & E. P. Kontar 2012; M. C. M. Cheung et al. 2015). However, not only is the AIA EUV intensity of the present target low, but there is also a bright 171 Å EUV loop located in the foreground of the jet, which may add unwanted contamination to the jet source. For this reason, we compare the DEMs derived from EUI/FSI images, which are less contaminated than features from AIA. FSI provides only two channels, which are practically inadequate for constraining DEM solutions. J. Youn et al. (2025) utilized a deep learning model based on Pix2PixCC (H.-J. Jeong et al. 2022) to be able to reproduce the five AIA channel (94, 193, 211, 131, and 335 Å) images from FSI 174 and 304 Å images. They determined the DEM by applying the standard procedure to this full set of the five AIA-equivalent images plus the original FSI 174 Å images. The resulting DEMs agree well with those derived from actual AIA observations across various temperature ranges. We therefore applied this technique to the FSI data to obtain the DEM results presented here.

Figure 5 shows the AIA-like five-channel data set generated using deep learning (hereafter AI-EUI), the EUV images observed by EUI$_{\mathrm{FSI}}$ at 174 Å, and the corresponding derived

DEMs. The error bars from the DEM plots are given by the I. G. Hannah & E. P. Kontar (2012) method, using AIA and EUI data manuals (P. Boerner et al. 2012; P. Rochus et al. 2020), and include the errors from the jet maximum period (19:10 UT) images and those of the jet quiet time (19:20 UT) images as well. At the jet maximum period (19:10 UT), the AIA DEM shows a peak at $\log T \approx 6.0$, whereas the AI-EUI DEM shows a peak at $\log T \approx 6.2$. The former peak includes an extra component coming from the foreground coronal loop in the AIA's viewpoint, whereas the latter must be the temperature of the plasma surrounding the jet. There is another peak of DEM at $\log T \approx 7.1$. This high-temperature peak is found for both AIA and AI-EUI and is obvious at 19:10 UT, when the jet activity is strongest. The DEM around this temperature becomes low when the jets diminish at 19:20 UT, evidencing that this must be the temperature range of the hot jet.

We subtract the EUI/FSI intensity at a jet quiet time (19:20:50 UT) from that at the jet time (19:10:50 UT) to obtain the net DEM of the jet. Since the jets under current study are small and faint features, the background subtraction is tricky (e.g., Q. M. Zhang & H. S. Ji 2014). We thus keep comparing AI-EUI results with those of AIA to check if the same trend is found in both results. If they behave similarly, we finally adopt the AI-EUI's results for DEM. We then calculate, from the net DEM, the emission measure of the jets, $\mathrm{EM} = \sum_i \mathrm{DEM}(\log T_i)\Delta \log T_i$, in the temperature range $4.0 \leqslant \log T \leqslant 8.0$ in the interval of $\Delta \log T = 0.1$. The median EM value over the jet area is calculated as $5.5 \times 10^{27}\ \mathrm{cm}^{-5}$ (lower right panel of Figure 5).

Note that the jet is so small, and its area on the EUI/FSI image is only 4 pixels wide. To determine the geometrical factors of the jet, we can no longer use the EUI/FSI images but must use the EUI/HRI$_{\mathrm{EUV}}$ images instead. Although the jet is of a highly entangled structure, we find that the 30% contour level of the maximum intensity of the EUI/HRI$_{\mathrm{EUV}}$ 174 Å image well outlines the jet area. On the EUI/HRI$_{\mathrm{EUV}}$ image, we count 475 pixels within the jet area, which amounts to $A \approx 1.0 \times 10^{17}\ \mathrm{cm}^2$. The average width of the jet strands is about 5 pixels or $w \approx 7.3 \times 10^7$ cm. In the regions where individual strands are resolved, we take w as the same as their LOS thickness, h. In the lower part of the jets, many strands are entangled, where we increase h according to the area of the brightened area. In this way, we determine the total number of electrons, $N = (\mathrm{EM}/h)^{1/2} A h \approx 2.0 \times 10^{35}$, and the total mass of the fully ionized plasma, $M = 1.1 N m_{\mathrm{H}} \approx 3.7 \times 10^{11}$ g. The thermal energy of the jet is then estimated as $3 N k_{\mathrm{B}} \langle T \rangle \approx 1.7 \times 10^{26}$ erg, where k_{B} is the Boltzmann constant and $\langle T \rangle$ is the DEM-weighted temperature. The kinetic energy of the jet is $M v^2/2 \approx 2.2 \times 10^{25}$ erg, using the mass, M, and the jet speed, $v = 110\ \mathrm{km\ s}^{-1}$. The total energy of the EUV jet therefore amounts to 1.9×10^{26} erg, with 87% in thermal energy and 13% in kinetic energy.

3. Discussion

This rare collaboration between EUI/HRI and GST/VIS presents a picture that the upwardly propagating EUV jets in the corona and the Hα redshift in the chromosphere are adjoined at the X-point. The hypothesis of the interchange reconnection in the corona is supported by the location and timing of multipolarity patches in the photosphere without magnetic flux cancellation and footpoint brightenings. However, straight trajectories of the ambient Hα spicules are in sharp contrast with the helical EUV jets, posing a puzzle regarding the role of magnetic reconnection in coronal jets and chromospheric ejections. We briefly discuss this issue based on two highly relevant models for small-scale jets, both of which self-consistently incorporate the chromosphere and corona within a unified framework (H. Iijima & T. Yokoyama 2017; D. Longcope & P. Klaassen 2025).

The chromospheric jet model proposed by H. Iijima & T. Yokoyama (2017) includes the photospheric radiative transfer and the equations of state in the simulation of the chromospheric jets. The most attractive feature of this model is that it predicts formation jets in the scales close to the present observation; specifically, the simulated jets consist of finer strands packed with a maximum height of 10–11 Mm and lifetime of 8–10 minutes in a cluster with a diameter of several Mm. The jets in this model are driven by the Lorentz force from the magnetic field lines strongly entangled in the chromosphere, which is somewhat inconsistent with the straight trajectories of Hα spicules although more appropriate for the EUV jet structure in the corona.

The reconnection model of D. Longcope & P. Klaassen (2025) considers impulsive, localized interchange reconnection in the low corona, as illustrated in Figure 6. Following its formation by reconnection, the field line straightens under tension (i.e., the Lorentz force). The straightening process consists of large-amplitude Alfvén waves propagating up and down, away from the reconnection site (see Figure 6(a)). The propagating waves produce parallel flows that collide to form a high-temperature, high-density central plug between them (D. W. Longcope et al. 2009; D. W. Longcope & S. E. Guidoni 2011; D. W. Longcope & J. A. Klimchuk 2015). The reconnection between a closed and an open field line (red semicircle and blue vertical line, respectively, in the left snapshot of Figure 6(a)) is asymmetric due to the significant plasma pressure difference between them. This asymmetry causes the plug to move upward, although at a speed somewhat slower than the Alfvén speed in either field. (Note how the upper bend in Figure 6(a) runs past the dashed line.)

The downward Alfvén wave impacts the chromosphere, where it drives cool, dense plasma upward to form a spicule (D. Longcope & P. Klaassen 2025; see Figure 6(c)). This occurs later, when the field line has almost entirely relaxed, leading to a much straighter plasma than the EUV loop. The upflow is much slower (by almost an order of magnitude in the illustrative example), causing it to reach its apex 4 minutes after reconnection.

The model is illustrated in Figure 6 using a thin flux tube simulation (S. E. Guidoni & D. W. Longcope 2010; D. W. Longcope & J. A. Klimchuk 2015; D. Longcope & P. Klaassen 2025) whose parameters have not been tuned to match the observation. Nevertheless, the example shows the rough magnitudes of its various components. The hot, dense plug moves upward at a fraction of the Alfvén speed, consistent with the $110\ \mathrm{km\ s}^{-1}$ that the observed EUV jets move across the plane of the sky. Moreover, its structuring by the evolving post-reconnection field gives the EUV loop an angle relative to the dominant open field. Our simulation considers the evolution of untwisted field lines confined to a plane (D. Longcope & P. Klaassen 2025), leaving the EUV jet with a distortion but not a helical twist. A more complicated scenario, with a twist in the initial and/or final field, could exhibit more properly helical distortion in the EUV loops during this initial phase of relaxation.

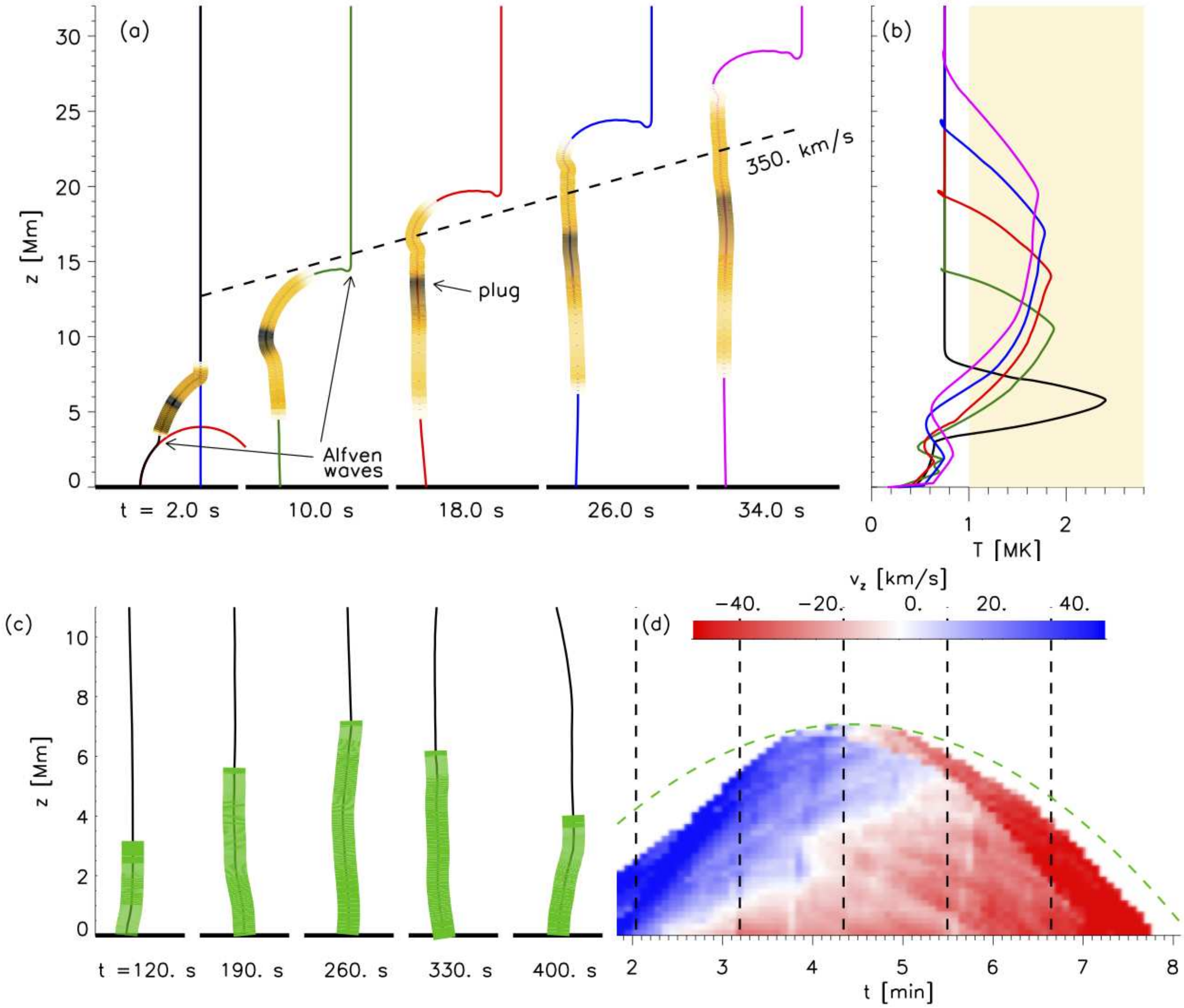

Figure 6. The reconnection model illustrated using a thin flux tube simulation. (a) Five snapshots from the initial phase in which the field line (colored curve) relaxes following its formation by reconnection. The pre-reconnection field lines are shown as red and blue curves in the leftmost snapshot. The reverse color scale shows emission measure of hot ($T > 10^6$ K) plasma. A dashed diagonal line shows a constant velocity, for reference. (b) The temperature vs. height for the five times using the same colors. The shaded box indicates the hot plasma whose emission is shown in (a). (c) At five later times, a spicule has been launched by the downward Alfvén wave. The green region shows cool ($<10^5$ K), dense plasma at each time. (d) The vertical velocity (shaded) in spacetime coordinates. A green dashed parabola shows freefall for reference, and vertical dashed lines show the times of the snapshots.

The same simulation exhibits a spicule when cool, dense plasma is launched upward by the impact of the downward Alfvén wave on the chromosphere. The cool plasma travels at $\sim$40 km s^{-1}, reaching a peak of 7 Mm before falling back under gravity. This is in line with the Doppler shifts and lengths of the Hα observations. The cooler plasma follows the relaxed field, making it much straighter, and more vertical, than the EUV loop, consistent with observations.

Under this model, reconnection releases energy by decreasing the length of the field line by ΔL. A closed loop with a mean field strength B_0, reconnecting to an open field, will release $W_{\rm mag}/\Phi = B_0\Delta L/4\pi$ (D. W. Longcope & J. A. Klimchuk 2015; D. Longcope & P. Klaassen 2025). For a rough estimate, we consider a loop connecting the parasitic polarity to the nearest negative region with a measured separation of 1.6 Mm (Figure 4(g)). This separation maps to a semicircle of radius $r = 0.80$ Mm, which would therefore be the height of the reconnection point. Due to this very low loop, we take $B_0 \simeq 130$ G, the average between the photospheric field strengths of the two polarity peaks ($\sim$+80 G and −180 G). Transforming a quarter circle to a vertical segment of the same height, r, shortens the tube by $\Delta L = (\pi/2 - 1)r = 0.46$ Mm. Such a shortening releases $W_{\rm mag}/\Phi \simeq 5.3 \times 10^8$ erg Mx^{-1}. The $w = 0.73$ Mm diameter loop will have flux $\Phi = B_0\pi(w/2)^2 = 5.4 \times 10^{17}$ Mx and therefore receive $W_{\rm mag} = 2.6 \times 10^{26}$ erg from reconnection. This will be shared between the EUV jet and the spicules and is therefore roughly consistent with our estimate of the energy in the jet alone (Section 2.5).

4. Concluding Remarks

The first joint observations of small-scale EUV jets using SoIO's EUI/HRI$_{\rm EUV}$ and BBSO's GST/VIS Hα during the 2022 October campaign for the Parker Solar Probe, we had a unique opportunity to directly compare the small, short-duration EUV jets with abundant Hα spicules in unprecedented detail. The observations and diagnostic results are summarized in the abstract and will not be repeated here. Here we wish to remark on the main issue: what dictates the structure and dynamics of the resulting SSEs in the chromosphere and the corona. The interchange reconnection as a trigger of the jet activity is unambiguously determined from the location of the EUV jets and Hα spicules relative to the photospheric magnetic fields, However, we encountered two unexpected puzzles: how the entangled structure forms and why it exclusively appears in the EUV wavelengths, not in the Hα line. All Hα features accompanying the EUV jets, including the sheath flow, bulk downflow, and normal upward spicules, exhibit straight trajectories.

Among the alternatives, the reconnection model, which begins with interchange reconnection, suggests some explanations. The twisted, or nonaligned, EUV structures form promptly in the corona as a result of the reconnection energy release there. Prompt heating and compressions make visible plasma, which had previously not been hot enough or dense enough to appear in EUV. Our demonstration, with a simplified geometry, exhibits a distorted EUV loop, but a more complicated configuration could exhibit helices. The compressed and heated plasma plug will move along the reconnected loop at a speed comparable to, but somewhat slower than, the Alfvén speed, in agreement with our observation. Finally, the cooler Hα feature forms through a secondary response to the episode of interchange reconnection after the downward Alfvén wave impacts the chromosphere. This plasma moves upward much more slowly and along the field that has already fully relaxed to become straight and vertical. The plasma at the feet appears to be redshifted at first, owing to chromospheric condensation, and later when the cool plasma drains back down.

To compare with other small jets detected by EUI/HRI$_{\rm EUV}$, the picoflare jets have kinetic energies below 10^{24} erg (L. P. Chitta et al. 2023), at least 2 orders of magnitude lower than that of the jet studied here. Despite this energy discrepancy, they share similar spatial scales, lifetimes, and velocities. Similarly, the helical EUI/HRI$_{\rm EUV}$ jet studied by E. Petrova et al. (2024) displays a comparable morphology and was also interpreted as propagating torsional Alfvén waves in a low coronal structure with an estimated wave energy flux of $140\,{\rm kW\,m^{-2}}$. If we tentatively calculate the corresponding kinetic energy of the Alfvénic pulse with an assumed loop diameter of 2 Mm and lifetime of 2 minutes, we find 5.3×10^{26} erg. In contrast, we estimated the total energy of the present jet as $\sim 1.9 \times 10^{26}$ erg, with 87% in thermal energy and 13% in kinetic energy, based on the DEM analysis as well as the NIRIS measurements of the footpoint separation of $\sim 2''$ and magnetic flux of $\sim 10^{17}$ Mx. All these jets are interpreted as powered by magnetic reconnection at the smallest scales of magnetic elements detectable in the quiet Sun (C. E. Parnell et al. 2009; J. Lee et al. 2025).

The results of this collaboration highlight the critical role of high-resolution GST observations in bridging the gap between the photosphere and corona by providing spectroscopic data on chromospheric dynamics alongside fine-structured coronal jets. These findings boosts SolO's objective of advancing our understanding of how the Sun generates SSEs in the chromosphere and corona, ultimately enhancing models of solar-heliospheric connections.

Acknowledgments

We wish to thank the referee for very thoughtful and helpful comments. We gratefully acknowledge the use of data from the Goode Solar Telescope (GST) of the Big Bear Solar Observatory (BBSO). BBSO operation is supported by US NSF grant AGS-2309939 and the New Jersey Institute of Technology. GST operation is partly supported by the Korea Astronomy and Space Science Institute and the Seoul National University. Solar Orbiter is a space mission of international collaboration between ESA and NASA, operated by ESA. The EUI instrument was built by CSL, IAS, MPS, MSSL/UCL, PMOD/WRC, ROB, and LCF/IO with funding from the Belgian Federal Science Policy Office (BELSPO/PRODEX PEA 4000112292); the Centre National d'Etudes Spatiales (CNES); the UK Space Agency (UKSA); the Bundesministerium für Wirtschaft und Energie (BMWi) through the Deutsches Zentrum für Luft- und Raumfahrt (DLR); and the Swiss Space Office (SSO). This work was supported by NSF grants AGS-2114201, AGS-2229064 and AGS-2309939 and NASA grants 80NSSC19K0257, 80NSSC20K0025, 80NSSC20K1282, 80NSSC24K1914, and 80NSSC24K0258. N. K.P. acknowledges support from NASA's SDO/AIA grant and NSF AAG award (No. 2307505). We acknowledge the use of SDO/AIA/HMI data. AIA is an instrument on board the Solar Dynamics Observatory, a mission for NASA's Living With a Star program.

Facilities: SolO (EUI), SDO (AIA, HMI), BBSO (GST/VIS and GST/NIRIS).

Software: IDL, SolarSoft (S. L. Freeland & B. N. Handy 2012), OF and DopplerCG (X. Yang et al. 2022).

ORCID iDs

Jeongwoo Lee https://orcid.org/0000-0002-5865-7924
Junmu Youn https://orcid.org/0009-0008-6476-054X
Navdeep K. Panesar https://orcid.org/0000-0001-7620-362X
Nengyi Huang https://orcid.org/0000-0001-9049-0653
Haimin Wang https://orcid.org/0000-0002-5233-565X

References

Beckers, J. M. 1977, in Illustrated Glossary for Solar and Solar-Terrestrial Physics, Astrophysics and Space Science Library, ed. A. Bruzek & C. J. Durrant, Vol. 69, 21
Berghmans, D., Auchère, F., Long, D. M., et al. 2021, A&A, 656, L4
Bizien, N., Froment, C., Madjarska, M. S., Dudok de Wit, T., & Velli, M. 2025, A&A, 694, A181
Boerner, P., Edwards, C., Lemen, J., et al. 2012, SoPh, 275, 41
Bohlin, J. D., Vogel, S. N., Purcell, J. D., et al. 1975, ApJL, 197, L133
Brueckner, G. E. 1982, BAAS, 14, 411
Cheung, M. C. M., Boerner, P., Schrijver, C. J., et al. 2015, ApJ, 807, 143
Chitta, L. P., Zhukov, A. N., Berghmans, D., et al. 2023, Sci, 381, 867
Cook, J. W., Brueckner, G. E., & Bartoe, J. D. F. 1983, ApJL, 270, L89
De Pontieu, B., Title, A. M., Lemen, J. R., et al. 2014, SoPh, 289, 2733
Dere, K. P., Bartoe, J. D. F., & Brueckner, G. E. 1989a, SoPh, 123, 41
Dere, K. P., Bartoe, J. D. F., Brueckner, G. E., et al. 1989b, SoPh, 119, 55
Freeland, S. L., & Handy, B. N., 2012 SolarSoft: Programming and Data Analysis Environment for Solar Physics, Astrophysics Source Code Library, ascl:1208.013
Goode, P. R., Yurchyshyn, V., Cao, W., et al. 2010, ApJL, 714, L31
Guidoni, S. E., & Longcope, D. W. 2010, ApJ, 718, 1476
Hannah, I. G., & Kontar, E. P. 2012, A&A, 539, A146
Iijima, H., & Yokoyama, T. 2017, ApJ, 848, 38
Jeong, H.-J., Moon, Y.-J., Park, E., Lee, H., & Baek, J.-H. 2022, ApJS, 262, 50
Karovska, M., & Habbal, S. R. 1994, ApJL, 431, L59
Lee, J., Georgoulis, M. K., Sharma, R., et al. 2025, ApJL, 988, L16
Lee, J., Yurchyshyn, V., Wang, H., et al. 2022, ApJL, 935, L27
Longcope, D., & Klaassen, P. 2025, ApJ, 989, 152

Longcope, D. W., & Guidoni, S. E. 2011, ApJ, 740, 73

Longcope, D. W., Guidoni, S. E., & Linton, M. G. 2009, ApJL, 690, L18

Longcope, D. W., & Klimchuk, J. A. 2015, ApJ, 813, 131

Mandal, S., Peter, H., Chitta, L. P., et al. 2023, A&A, 670, L3

Moore, R. L., Tang, F., Bohlin, J. D., & Golub, L. 1977, ApJ, 218, 286

Müller, D., St. Cyr, O. C., Zouganelis, I., et al. 2020, A&A, 642, A1

Panesar, N. K., Hansteen, V. H. H., Tiwari, S. K., et al. 2023, ApJ, 943, 24

Panesar, N. K., Sterling, A. C., Moore, R. L., et al. 2018, ApJL, 868, L27

Panesar, N. K., Sterling, A. C., Moore, R. L., et al. 2019, ApJL, 887, L8

Panesar, N. K., Tiwari, S. K., Berghmans, D., et al. 2021, ApJL, 921, L20

Parnell, C. E., DeForest, C. E., Hagenaar, H. J., et al. 2009, ApJ, 698, 75

Petrova, E., Van Doorsselaere, T., Berghmans, D., et al. 2024, A&A, 687, A13

Raouafi, N. E., Patsourakos, S., Pariat, E., et al. 2016, SSRv, 201, 1

Raouafi, N.-E., & Stenborg, G. 2014, ApJ, 787, 118

Raouafi, N. E., Stenborg, G., Seaton, D. B., et al. 2023, ApJ, 945, 28

Rochus, P., Auchère, F., Berghmans, D., et al. 2020, A&A, 642, A8

Rouppe van der Voort, L., Leenaarts, J., de Pontieu, B., Carlsson, M., & Vissers, G. 2009, ApJ, 705, 272

Samanta, T., Tian, H., Yurchyshyn, V., et al. 2019, Sci, 366, 890

Shen, Y. 2021, RSPSA, 477, 20200217

Shi, F., Li, D., Ning, Z., et al. 2024, A&A, 686, A279

Shibata, K., Ishido, Y., Acton, L. W., et al. 1992, PASJ, 44, L173

Sterling, A. C., Moore, R. L., Falconer, D. A., et al. 2016, ApJ, 821, 100

Sterling, A. C., Panesar, N. K., & Moore, R. L. 2024, ApJ, 963, 4

Tandberg-Hanssen, E. 1977, in Illustrated Glossary for Solar and Solar-Terrestrial Physics, Astrophysics and Space Science Library, ed. A. Bruzek & C. J. Durrant, Vol. 69, 97

Tian, H., Kleint, L., Peter, H., et al. 2014, ApJL, 790, L29

Uitenbroek, H. 2003, ApJ, 592, 1225

Yamauchi, Y., Moore, R. L., Suess, S. T., Wang, H., & Sakurai, T. 2004, ApJ, 605, 511

Yamauchi, Y., Wang, H., Jiang, Y., Schwadron, N., & Moore, R. L. 2005, ApJ, 629, 572

Yang, X., Cao, W., & Yurchyshyn, V. 2022, ApJS, 262, 55

Youn, J., Lee, H., Jeong, H.-J., et al. 2025, A&A, 695, A125

Zhang, Q. M., & Ji, H. S. 2014, A&A, 567, A11